Real-time dynamics in spin-$\frac{1}{2}$ chains with adaptive time-dependent density matrix renormalization group

Dominique Gobert,[1,2] Corinna Kollath,[1,2] Ulrich Schollwöck,[1] and Gunter Schütz[3]
[1]*Institute for Theoretical Physics C, RWTH Aachen, D-52056 Aachen, Germany*
[2]*Physics Department and CeNS, LMU München, Theresienstrasse 37, D-80333 München, Germany*
[3]*Institut für Festkörperforschung, Forschungszentrum Jülich, D-52425 Jülich, Germany*
(Received 7 October 2004; published 3 March 2005)

We investigate the influence of different interaction strengths and dimerizations on the magnetization transport in antiferromagnetic spin 1/2 *XXZ* chains. We focus on the real-time evolution of the inhomogeneous initial state $|\uparrow\cdots\uparrow\downarrow\cdots\downarrow\rangle$ in using the adaptive time-dependent density-matrix renormalization group (adaptive t-DMRG). Time scales accessible to us are of the order of 100 units of time measured in $\hbar/J$ for almost negligible error in the observables. We find ballistic magnetization transport for small S^zS^z interaction and arbitrary dimerization, but almost no transport for stronger S^zS^z interaction, with a sharp crossover at $J^z=1$. Additionally, we perform a detailed analysis of the error made by the adaptive time-dependent DMRG using the fact that the evolution in the *XX* model is known exactly. We find that the error at small times is dominated by the error made by the Trotter decomposition, whereas for longer times the DMRG truncation error becomes the most important, with a very sharp crossover at some "runaway" time. Overall, errors are extremely small before the "runaway" time.

DOI: 10.1103/PhysRevE.71.036102 PACS number(s): 05.50.+q

I. INTRODUCTION

The transport properties of spin chains have attracted much attention recently, not only due to the possible applications to information storage, spintronics, and quantum information processing, but also because they allow us to study general aspects of nonequilibrium dynamics in a comparably simple system. Nonequilibrium phenomena are a vast and, despite all progress, still poorly understood field of statistical physics. It is therefore useful to have a simple model at hand that allows us to study general questions rather explicitly. In order to study nonequilibrium phenomena, a real-time description is particularly intuitive and useful. In this paper, we study the time evolution of a spin-$\frac{1}{2}$ chain by solving the full many-body Schrödinger equation.

Recently, new developments in the area of nonequilibrium physics were stimulated by the experimental progress in the field of ultracold atoms. These systems have the advantage that their parameters can be tuned in time with high accuracy and on very short time scales. It was proposed that spin-$\frac{1}{2}$ chains can be realized in these systems as well [1–4], namely as a mixture of atoms of two species, say *A* and *B*. If these atoms are studied in an optical lattice with an average filling of one atom per site and with a very strong repulsive interaction between the atoms, such that multiple occupancy is suppressed, the system can be mapped onto an effective spin-$\frac{1}{2}$ model. In this effective model, the state with atom *A* occupying a given lattice site corresponds to, say, $\uparrow$, and likewise *B* to $\downarrow$.

In this paper, we study the time evolution of an initial state $|\uparrow\cdots\uparrow\downarrow\cdots\downarrow\rangle$ (or $|A\cdots AB\cdots B\rangle$), i.e., with all spins on the left half pointing up along the *z* axis, and all spins on the right half pointing down, under the effect of a nearest-neighbor spin interaction [see Eq. (1)]. This system can also be interpreted as an oversimplified picture for spin transport between two coupled reservoirs of completely polarized spins of opposite direction in the two reservoirs. We are mainly interested in the following questions: Does the state evolve into a simple long-time limit? If so, how is this limit reached? On what properties does the long-time behavior depend?

Analytical results for this problem are essentially restricted to the *XX* chain with and without dimerization which is amenable to an exact solution [5,6]. In Ref. [5], a scaling relation for the long-time limit was found. However, it is presently not known whether this relation is general or whether it relies on special properties of the *XX* model. If a long-time limit exists for other models as well, the question arises as to which of its characteristics are universal, and which depend on certain system properties.

Directly solving the time-dependent Schrödinger equation for interacting many-body systems is highly nontrivial. A recently developed numerical method, the adaptive time-dependent DMRG [7–9] (adaptive t-DMRG), enables us to perform this task. The two main conditions for this method to be applicable, namely that the system must be one-dimensional and have nearest-neighbor interactions only, are met for the present model. Efforts to generalize the DMRG method to time-dependent problems relaxing these constraints are under way [10].

As so far no detailed error analysis of this new method has been performed, an important aspect of the present work is that besides their own physical interest, spin-$\frac{1}{2}$ chains provide an excellent benchmark for the adaptive time-dependent DMRG, because of the nontrivial exact solution for the *XX* model, against which the method can be compared. This allows us to analyze the accuracy of the adaptive time-dependent DMRG very explicitly, namely to address the questions of what kinds of errors can occur in principle, which ones of these dominate in practice, and how they can

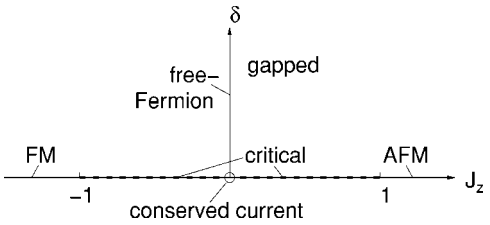

FIG. 1. Quantum phase diagram of the Heisenberg model, Eq. (1). See [11,12] for details.

be minimized. We find that the time scales accessible to us are about $100\hbar/J$, with a neglegible error in the observables at very moderate numerical cost.

The outline of our paper is as follows. In Sec. II, we introduce the model and its characteristics. In Sec. III, we summarize the method, and in Sec. IV a detailed error analysis is performed. These two sections may be skipped by readers mainly interested in the physics and not in the details of the method. In Sec. V, we present our results for the long-time limit of the time evolution for different interaction and dimerization strength.

II. MODEL AND INITIAL STATE

In this paper, we analyze the dynamics of the inhomogeneous initial state $|\mathrm{ini}\rangle = |\uparrow\cdots\uparrow\downarrow\cdots\downarrow\rangle$ on the one-dimensional spin-$\frac{1}{2}$ chains with interactions given by the Heisenberg model

$$H = \sum_n J_n (S_n^x S_{n+1}^x + S_n^y S_{n+1}^y + J_z S_n^z S_{n+1}^z) \equiv \sum_n h_n. \qquad (1)$$

Here, $\vec{S}_n$ is the spin operator on site n, and J_n, J_z are interaction constants. We consider dimerized models where $J^z = \mathrm{const}$ and $J_n = [1 + (-1)^n \delta]$, δ being the dimerization coefficient. For $\delta > 0$, the "strong bond" with $J_n = 1 + \delta$ is chosen to be at the center, where the spin flip of the initial state is located.

We have chosen our energy unit such that $J_n = 1$ for the homogeneous case $\delta = 0$. We also set $\hbar = 1$, defining time to be $1/\mathrm{energy}$ with the energy unit chosen as just mentioned.

The quantum phase diagram of this model at zero temperature is well known (see [11,12]) and sketched in Fig. 1. For the homogeneous case, $\delta = 0$, the ground state has ferromagnetic (FM) / antiferromagnetic (AFM) order with a gap in the excitation spectrum for $J_z < -1$ and $J_z > 1$, respectively. The gap closes if $|J_z|$ approaches 1 from above, and the model becomes critical for $-1 < J_z < 1$, i.e., gapless in the thermodynamic limit, with correlation functions showing a power-law decay. The model at the point $J_z = \delta = 0$ is known as the *XX* model. It has the special property that the spin-current operator $J = \Sigma_n j_n$ is conserved, i.e., $[J, H] = 0$. Here $j_n = J_n \mathrm{Im}(S_n^+ S_{n+1}^-)$ is the current operator on the bond between site n and $n+1$. For finite dimerization, $\delta \neq 0$, the spectrum is again gapped for all values of J_z.

Often it is useful to map the Heisenberg model onto a model of spinless fermions,

$$H = \sum_n J_n \left[\frac{1}{2}(c_n^\dagger c_{n+1} + c_{n+1}^\dagger c_n) + J_z \left(c_n^\dagger c_n - \frac{1}{2} \right) \left(c_{n+1}^\dagger c_{n+1} - \frac{1}{2} \right) \right]. \qquad (2)$$

In this picture, the first two terms in Eq. (1) describe nearest-neighbor hopping, whereas the third term (the one proportional to J_z) describes a density-density interaction between nearest neighbors. In particular, the case $J_z = 0$ describes free fermions on a lattice, and can be solved exactly [13].

The time evolution under the influence of a time-independent Hamiltonian H as in Eq. (1) is given by

$$|\psi(t)\rangle = U(t)|\mathrm{ini}\rangle \quad \text{with } U(t) = \exp(-iHt). \qquad (3)$$

In most of the phases shown in Fig. 1, the state $|\mathrm{ini}\rangle = |\uparrow\cdots\uparrow\downarrow\cdots\downarrow\rangle$ contains many high-energy excitations and is thus far from equilibrium. In the following, we briefly discuss these phases separately.

(i) Deep in the ferromagnetic phase, $J_z < -1$, $|\mathrm{ini}\rangle$ corresponds to a state with one domain wall between the two degenerate ground states. For $J_z \to -\infty$, it is identical to the ground state (with boundary conditions given by $|\uparrow\rangle$ and $|\downarrow\rangle$ and $S_z^{\mathrm{tot}} = 0$), and therefore stationary. For finite J_z, it is no longer identical to the ground state, but still close to it [14].

(ii) In the antiferromagnetic phase, $J_z > 1$, the state $|\mathrm{ini}\rangle$ is highly excited. One could view it as a state with almost the maximum number of domain walls of staggered magnetization.

In this context, it is interesting to note that the sign of J_z does not matter for the time evolution of physical quantities, as long as the initial state is described by a purely real wave function (which is the case for our choice of $|\mathrm{ini}\rangle$), since the sign change in J_z can be compensated by a gauge transformation that inverts the sign of the hopping terms $S^x S^x$, $S^y S^y$ in Eq. (1), plus a complex conjugation of Eq. (3). In particular, the time evolution of the low-energy one-domain-wall state in the FM is the same as the evolution of the high-energy many-domain-walls state in the AFM. We therefore restrict ourselves to the case $J_z > 0$.

(iii) In the critical phase $\delta = 0$ and $|J_z| < 1$, the ground state is a state with power-law correlations in the *xy* plane. Here, the state $|\mathrm{ini}\rangle$ is not close to any particular eigenstate of the system, but contains many excited states throughout the energy spectrum, depending on the value of J_z: The energy expectation value of $|\mathrm{ini}\rangle$ is low as $J^z \to -1$ and high as $J^z \to 1$.

The time evolution delocalizes the domain wall over the entire chain. For $J_z = 0$, the time evolution of the system can be solved exactly. For example, the magnetization profile for the initial state $|\mathrm{ini}\rangle$ reads [5]

$$S_z(n,t) = \langle \psi(t)|S_n^z|\psi(t)\rangle = -1/2 \sum_{j=1-n}^{n-1} J_j^2(t), \qquad (4)$$

where J_j is the Bessel function of the first kind. $n = \ldots, -3, -2, -1, 0, 1, 2, 3, \ldots$ labels chain sites with the convention that the first site in the right half of the chain has the label $n = 1$.

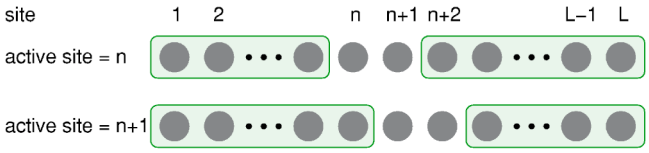

FIG. 2. Illustration of the DMRG bases with active site n and $n+1$, respectively.

(iv) In the dimerized phase, $\delta \neq 0$, the mentioned characteristics remain unchanged. However, here the delocalization becomes confined to pairs of neighboring sites in the limit $\delta \to 1$.

We finally note that the total energy and magnetization of the system are conserved at all times, such that even for long times the state cannot relax to the ground state.

III. OUTLINE OF THE ADAPTIVE TIME-DEPENDENT DMRG FOR SPIN CHAINS

In order to determine the time evolution of Eq. (3), we use the adaptive t-DMRG method [8,9], which has been introduced as an extension of standard DMRG using the TEBD algorithm of Vidal [7]. It allows us to evaluate the time evolution for one-dimensional quantum chains with nearest-neighbor (possibly time-dependent) interactions. In this paper, we consider the case of a time-independent Hamiltonian where the dynamics is introduced by a nonequilibrium initial state at $t=0$. To set the stage for the error analysis, we briefly review adaptive t-DMRG, assuming the reader to be familiar with standard static zero-temperature DMRG (see, e.g., [15,16]).

In the standard finite-system DMRG algorithm, a quantum-mechanical state on a one-dimensional chain with L sites is represented in a particular tensor product basis, namely as

$$|\psi\rangle = \sum_{\alpha\sigma\tau\beta} \psi_{\alpha\sigma\tau\beta} |\alpha\rangle_{1\cdots n-1} |\sigma\rangle_n |\tau\rangle_{n+1} |\beta\rangle_{n+2\cdots L} \tag{5}$$

as illustrated in the upper part of Fig. 2. Here, $|\sigma\rangle_n, |\tau\rangle_{n+1}$ are complete bases on sites $n, n+1$; $|\alpha\rangle_{1\cdots n-1}$ and $|\beta\rangle_{n+2\cdots L}$ are states on the subchains with sites 1, …, $n-1$ and $n+2$, …, L, respectively. The states $|\alpha\rangle_{1\cdots n-1}$ and $|\beta\rangle_{n+2\cdots L}$ form truncated bases, i.e., they do not span the full Hilbert space on their respective subchains, but only a subspace of dimension m, chosen to allow an optimal approximation of the true physical state. In the representation of Eq. (5), we call site n the "active site." The algorithm now consists of moving ("sweeping") the position of the active site several times from the left to the right end of the chain and back, and constructing optimized truncated bases for the subchains.

A DMRG step during such a sweep, say to the right, now consists of a basis transformation from the old (truncated) basis $|\alpha\rangle_{1\cdots n-1}|\sigma\rangle_n|\tau\rangle_{n+1}|\beta\rangle_{n+2\cdots L}$ with active site n to a new one $|\alpha'\rangle_{1\cdots n}|\sigma'\rangle_{n+1}|\tau'\rangle_{n+2}|\beta'\rangle_{n+3\cdots L}$ with active site $n+1$, as shown in Fig. 2. The states $|\alpha'\rangle_{1\cdots n}$ representing the sites 1, …, n are linear combinations of the old basis vectors $|\alpha\rangle_{1\cdots n-1}|\sigma\rangle_n$. Not all linear combinations are kept because of the DMRG truncation that limits the number of states $|\alpha'\rangle_{1\cdots n}$ to m states. For this reason, the state $|\psi\rangle$ can in general be represented in the new basis only up to some truncation error. The DMRG truncation algorithm (described in [15,16]) provides a unique optimal choice for the states $|\alpha'\rangle$ that minimizes this error (which is then typically as low as 10^{-10} or so) and thus allows for the optimal representation of particular "target" states. The basis vectors $|\beta'\rangle_{n+3\cdots L}$ are taken from stored values from the previous sweep to the left. A sweep to the left (i.e., from active site n to $n-1$) works in the same way, with the role of $|\alpha'\rangle$ and $|\beta'\rangle$ interchanged.

In standard DMRG, a mere transformation of the state $|\psi\rangle$ from one basis to the other—known as White's state prediction [17]—is possible and accurate up to the (small) truncation error. However, in order to optimize the basis states iteratively for representing the target state(s) $|\psi\rangle$, new information must be provided about $|\psi\rangle$, i.e., it must be newly constructed using some unique criterion (typically as the ground state of some Hamiltonian). Without such a criterion to "sweep against," the accuracy cannot increase during sweeps, and the procedure would be pointless. Merely transforming $|\psi\rangle$ in this way is therefore of no use in standard DMRG, and is in fact never performed alone. It is, however, the basis of the adaptive t-DMRG.

The adaptive t-DMRG algorithm relies on the Trotter decomposition of the time-evolution operator $U(t)$ of Eq. (3), which is defined as follows: Using the relation $U(t) = U(dt=t/M)^M$, the time-evolution operator is decomposed into M time steps, where M is a large number such that the time interval $dt=t/M$ is small compared to the physical time scales of the model. Since the Hamilton operator of Eq. (1) can be decomposed into a sum of local terms h_n that live only on sites n and $n+1$, $U(dt)$ can then be approximated by an nth-order Trotter decomposition [18], e.g., to second order,

$$U(dt) = \prod_{\substack{n \\ \text{even}}} U_n\left(\frac{dt}{2}\right) \prod_{\substack{n \\ \text{odd}}} U_n(dt) \prod_{\substack{n \\ \text{even}}} U_n\left(\frac{dt}{2}\right) + O(dt^3). \tag{6}$$

The $U_n(dt)$ are the infinitesimal time-evolution operators $\exp(-ih_n dt)$ on the bonds n (even or odd). The ordering *within* the even and odd products does not matter, because "even" and "odd" operators commute among themselves.

Equation (6) allows us to decompose the time-evolution operator $U(t)$ into many local operators U_n that live on sites n and $n+1$. The adaptive time-dependent DMRG now allows us to apply the operators U_n successively to some state Ψ. Each operator U_n is applied exactly during sweeps in the DMRG step with n being the active site, i.e., where sites n and $n+1$ are represented without truncation [cf. Eq. (5)]: This way, the basis states chosen to represent optimally the state before U_n is applied,

$$|\psi\rangle = \sum_{\alpha\sigma\tau\beta} \psi_{\alpha\sigma\tau\beta} |\alpha\rangle |\sigma\rangle_n |\tau\rangle_{n+1} |\beta\rangle, \tag{7}$$

are equally well suited for representing the state

$$U_n|\psi\rangle = \sum_{\substack{\alpha\sigma\tau\beta \\ \sigma'\tau'}} (U_n)_{\sigma\tau,\sigma'\tau'} \psi_{\alpha\sigma'\tau'\beta} |\alpha\rangle|\sigma\rangle_n|\tau\rangle_{n+1}|\beta\rangle \qquad (8)$$

without any additional error, because U_n only acts on the part of the Hilbert space (spanned by the vectors $|\sigma\rangle_n|\tau\rangle_{n+1}$) that is exactly represented.

To continue the sweep, a DMRG truncation is carried out with $U_n|\psi\rangle$ being the target state instead of $|\psi\rangle$. The key observation is that the new truncated basis is optimally adapted to $U_n|\psi\rangle$ and different from the one that would have been chosen for $|\psi\rangle$. In contrast to the conventional static DMRG [19], the optimally represented Hilbert space hence *follows the time evolution of the state* $|\psi(t)\rangle$.

Then basis transformations to the left or right are performed, until the next part of Eq. (6) can be applied. We thus apply the full operator of Eq. (6) by sweeping the active site n through the system. The price to be paid is that a truncation error is introduced at each iteration step of the sweep as is known from static DMRG.

To start time-dependent DMRG, some initial state has to be prepared. There is no unique recipe, the most effective one depending on the desired initial state. The procedure we adopt for our initial state $|\mathrm{ini}\rangle$ is to calculate it as the ground state of a suitably chosen Hamiltonian H_{ini} (which in principle does not have to have any physical significance). Such a choice is $H_{\mathrm{ini}}=\Sigma_n B_n S_n^z$, with $B_n<0$ for n on the left, and $B_n>0$ for n on the right half of the chain. In this case, a physical picture for H_{ini} does exist; it corresponds to switching on a magnetic field that aligns the spins and that is strong enough for all interactions in Eq. (1) to be negligible.

IV. ACCURACY OF THE ADAPTIVE TIME-DEPENDENT DMRG

As so far no quantitative analysis of the accuracy of the adaptive t-DMRG has been given in the literature, we provide a detailed error analysis for the time evolution of the initial state $|\mathrm{ini}\rangle$ in a spin-$\frac{1}{2}$ quantum XX chain, i.e., $J_z=\delta=0$. This system is an excellent benchmark for the adaptive t-DMRG due to its exact solution [5] that can be compared to the DMRG results. The exact solution reveals a nontrivial behavior with a complicated substructure in the magnetization profile. From a DMRG point of view, this Hamiltonian is not too specific in the sense that the experience from static DMRG suggests a relatively weak truncation error dependence on J^z.

A. Possible errors

Two main sources of error occur in the adaptive t-DMRG.

(i) The *Trotter error* due to the Trotter decomposition. For an nth-order Trotter decomposition [18], the error made in one time step dt is of order dt^{n+1}. To reach a given time t, one has to perform t/dt time steps, such that in the worst case the error grows linearly in time t and the resulting error is of order $(dt)^n t$. In our setup of the Trotter decomposition, the error scales linearly with system size L, and overall it is of order $(dt)^n Lt$ for the times of interest. (Eventually, the error must saturate at a finite value, as measured quantities are typically bounded.) The linear L dependence of the error is expected for generic initial states. For the particular choice of $|\mathrm{ini}\rangle$ of this paper, however, many of the $O(L)$ contributions to the Trotter error vanish, as many of the sites exhibit no dynamics at all for short times. For the calculations presented in this paper, we have chosen $n=2$, but our observations should be generic.

(ii) The DMRG *truncation error* due to the representation of the time-evolving quantum state in reduced (albeit "optimally" chosen) Hilbert spaces and to the repeated transformations between different truncated basis sets. While the truncation error ϵ that sets the scale of the error of the wave function and operators is typically very small, here it will strongly accumulate as $O(Lt/dt)$ truncations are carried out up to time t. This is because the truncated DMRG wave function has norm less than 1 and is renormalized at each truncation by a factor of $(1-\epsilon)^{-1}>1$. Truncation errors should therefore accumulate roughly exponentially with an exponent of $\epsilon Lt/dt$, such that eventually the adaptive t-DMRG will break down at too long times. The error measure we use here saturates at $O(1)$ and sets a limit on the exponential growth; also, partial compensations of errors in observables may slow down the error growth. The accumulated truncation error should decrease considerably with an increasing number of kept DMRG states m. For a fixed time t, it should decrease as the Trotter time step dt is increased, as the number of truncations decreases with the number of time steps t/dt.

At this point, it is worthwhile to mention that our subsequent error analysis should also be pertinent to the very closely related time-evolution algorithm introduced by Verstraete *et al.* [20], which differs from ours for the present purpose in one major point: In our algorithm, a basis truncation is performed after each *local* application of U_n. In their algorithm, truncations are performed after all local time evolutions have been carried out, i.e., after a *global* time evolution using $U=\Pi_n U_n$. In our iterative procedure, the wave function after such a full time evolution is not guaranteed to be the *globally* optimal state representing the time-evolved state. However, for small dt, the state update via the operators U_n is likely to be small, so we expect the global optimum to be rather well approximated using the present algorithm, as seems to be borne out by direct comparisons between both approaches [21]. Errors should therefore exhibit very similar behavior.

We remind the reader that no error is encountered in the application of the local time-evolution operator U_n to the state $|\psi\rangle$, as is discussed after Eq. (8).

B. Error analysis for the *XX* model

In this section, we analyze the errors from the adaptive t-DMRG in the time evolution of the XX model by comparing it to the exact solution [5], with the ultimate goal of finding optimal DMRG control parameters to minimize the errors.

We use two main measures for the error.

(i) As a measure for the overall error, we consider the *magnetization deviation* the maximum deviation of the local

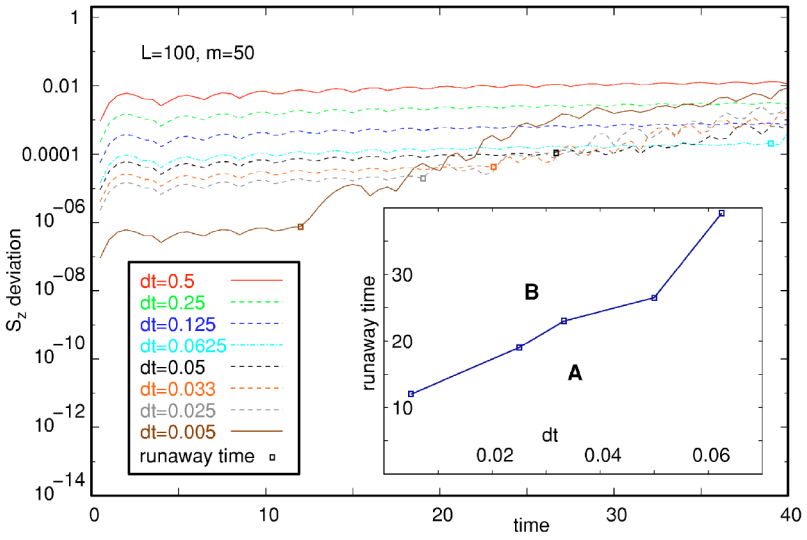

FIG. 3. Magnetization deviation as a function of time for different Trotter time steps dt and for $m=50$ DMRG states. At small times (region A in the inset), the deviation is dominated by the linearly growing Trotter error for small times. At later times (region B in the inset), much faster, nonlinear growth of the deviation sets in at some well-defined runaway time t_R. As shown in the inset, t_R increases with increasing dt.

magnetization found by DMRG from the exact result,

$$\Delta_{\max}(t) = \max_n |\langle S^z_{n,\mathrm{DMRG}}(t)\rangle - \langle S^z_{n,\mathrm{exact}}(t)\rangle|. \tag{9}$$

In the present study, the maximum was typically found close to the center of the chain.

(ii) As a measure which excludes the Trotter error, we use the *forth-back deviation* $\Delta_{\mathrm{FB}}(t)$, which we define as the deviation between the initial state $|\mathrm{ini}\rangle$ and the state $|\psi_{\mathrm{FB}}(t)\rangle = U(-t)U(t)|\mathrm{ini}\rangle$, i.e., the state obtained by evolving $|\mathrm{ini}\rangle$ to some time t and then back to $t=0$ again. If we Trotter-decompose the time evolution operator $U(-t)$ into odd and even bonds in the reverse order of the decomposition of $U(t)$, the identity $U(-t)=U(t)^{-1}$ holds without any Trotter error, and the forth-back deviation has the appealing property to capture the truncation error only. In contrast to the magnetization deviation, the forth-back error does not rely on the existence of an exact solution.

As our DMRG setup does not allow easy access to the fidelity $|\langle \mathrm{ini}|\psi_{\mathrm{FB}}(t)\rangle|$, we define the forth-back deviation to be the L_2 measure for the difference of the magnetization profiles of $|\mathrm{ini}\rangle$ and $|\psi_{\mathrm{FB}}(t)\rangle$,

$$\psi_{\mathrm{FB}}(t) = \left(\sum_n [\langle \mathrm{ini}|S^z_n|\mathrm{ini}\rangle - \langle \psi_{\mathrm{FB}}(t)|S^z_n|\psi_{\mathrm{FB}}(t)\rangle]^2\right)^{1/2}. \tag{10}$$

In order to control Trotter and truncation error, two DMRG control parameters are available, namely the number of DMRG states m and the Trotter time step dt.

To study the effect of varying dt, consider the *magnetization deviation* as shown in Fig. 3. Two main observations can be made. At small times (regime A), the magnetization deviation decreases with dt and is linear in t as expected from the Trotter error. Indeed, as shown in the upper part of Fig. 4, the magnetization deviation depends quadratically on dt for fixed t, and the Trotter error dominates over the truncation error. At large times (regime B), the magnetization deviation is no longer linear in t, but grows almost exponentially, and also no longer shows simple monotonic behavior in dt: The magnetization deviation in this regime is obviously no longer dominated by the Trotter error, but by the accumulated truncation error.

The two regimes A and B are very clearly separated by some *runaway time* t_R, with regime A for $t<t_R$ and regime B for $t>t_R$ (a precise procedure for its determination will be outlined below). The runaway time t_R increases when dt is increased: Because the total number of Trotter time steps t/dt is decreased, the accumulated truncation error decreases,

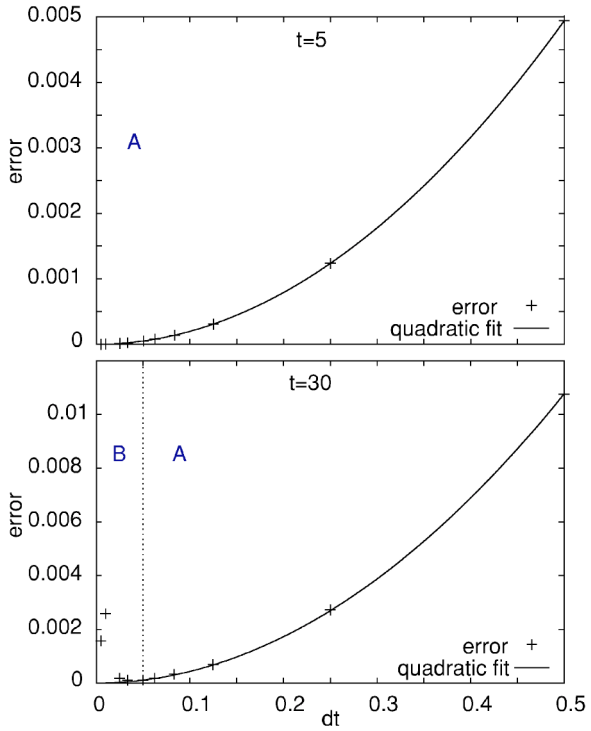

FIG. 4. Magnetization deviation as a function of Trotter time step dt (system size $L=100$, $m=50$ DMRG states) at times $t=5$ (upper figure) and $t=30$ (lower figure). For $t=5$, the magnetization deviation is quadratic in dt as expected from the Trotter error. For $t=30$, at small dt the magnetization deviation is no longer quadratic in dt and larger than the Trotter error would suggest. This is a signal of the contribution of the accumulated truncation error.

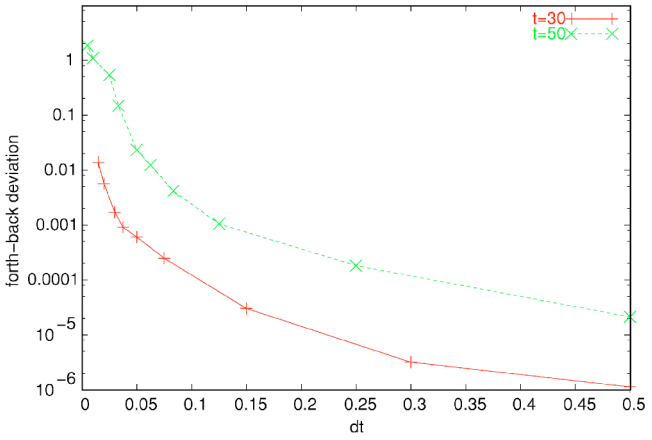

FIG. 5. The forth-back error $E_{\mathrm{FB}}(t)$ for $t=30$ and $t=50$ as a function of dt. Here, $L=100$, $m=50$.

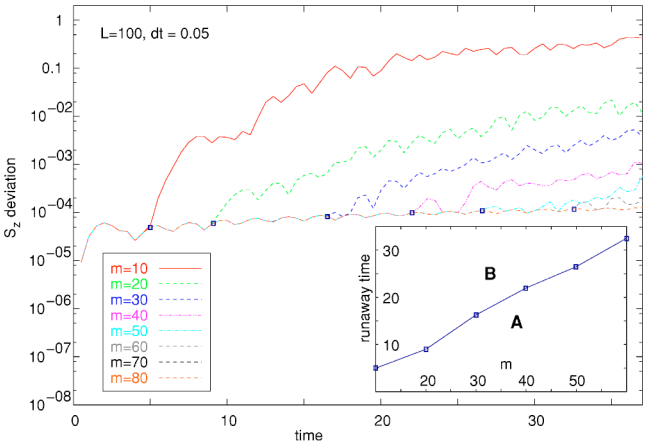

FIG. 6. Magnetization deviation $\Delta M(t)$ as a function of time for different numbers m of DMRG states. The Trotter time interval is fixed at $dt=0.05$. Again, two regimes can be distinguished: For early times, for which the Trotter error dominates, the error is slowly growing (essentially linearly) and independent of m (regime A); for later times, the error is entirely given by the truncation error, which is m-dependent and growing fast (almost exponential up to some saturation; regime B). The transition between the two regimes occurs at a well-defined "runaway time" t_R (small squares). The inset shows a monotonic, roughly linear dependence of t_R on m.

and the Trotter error increases, hence the competing two errors break even later.

This dt dependence of t_R is also seen in the lower part of Fig. 4, where the dt dependence of the magnetization deviation is plotted at some larger time ($t=30$) than in the upper part. $t=30$ is larger than the runaway time (i.e., in regime B) for $dt \leqslant 0.05$, in regime A otherwise. We see indeed for $dt > 0.05$ (region A) the familiar quadratic Trotter error dependence. For small $dt \leqslant 0.05$ (region B), the deviation is dominated by the accumulated truncation error that increases as dt decreases. This is reflected in the growth of the magnetization deviation as dt is decreased.

The almost exponential growth of the truncation error with the number of Trotter steps can also be seen from the forth-back deviation that is not susceptible to the Trotter error. In Fig. 5, we show the forth-back deviation $E_{\mathrm{FB}}(t)$ for $t=30$ and $t=50$ as a function of the Trotter time step dt. $E_{\mathrm{FB}}(t)$ increases as a consequence of the stronger accumulation of the truncation error with decreasing Trotter step size dt and hence an increasing number of steps t/dt.

Let us now consider the dependence of the magnetization deviation err(t) on the second control parameter, the number m of DMRG states. In Fig. 6, err(t) is plotted for a fixed Trotter time step $dt=0.05$ and different values of m. In agreement with our previous observations, some m-dependent "runaway time" t_R separates two regimes: for $t<t_R$ (regime A), the deviation grows essentially linearly in time and is independent of m; for $t>t_R$ (regime B), it suddenly starts to grow more rapidly than any power law. The onset of a significant m dependence has indeed been our operational definition of t_R in Figs. 3 and 6. In the inset of Fig. 6, t_R is seen to increase roughly linearly with growing m. As $m \to \infty$ corresponds to the complete absence of the truncation error, the m-independent bottom curve of Fig. 6 is a measure for the deviation due to the Trotter error alone and the runaway time can be read off very precisely as the moment in time when the truncation error starts to dominate.

That the crossover from a dominating Trotter error at short times and a dominating truncation error at long times is so sharp may seem surprising at first, but can be explained easily by observing that the Trotter error grows only linearly in time, but the accumulated truncation error grows almost exponentially in time. The latter fact is shown in Fig. 7, where the forth-back deviation $E_{\mathrm{FB}}(t)$ is plotted as a function of t for some fixed m. Here, we find that the effects of the truncation error are below machine precision for $t<10$ and then grow almost exponentially in time up to some saturation.

By comparison, consider Fig. 8, where $E_{\mathrm{FB}}(t)$ is plotted as a function of m, for $t=30$ and $t=50$. An approximately exponential increase of the accuracy of the method with growing m is observed for a fixed time. Our numerical results that indicate a roughly linear time dependence of t_R on m (inset of Fig. 6) are the consequence of some balancing of very fast growth of precision with m and decay of precision with t.

Before concluding this section, let us briefly consider a number of other possible effects that might affect t_R. One

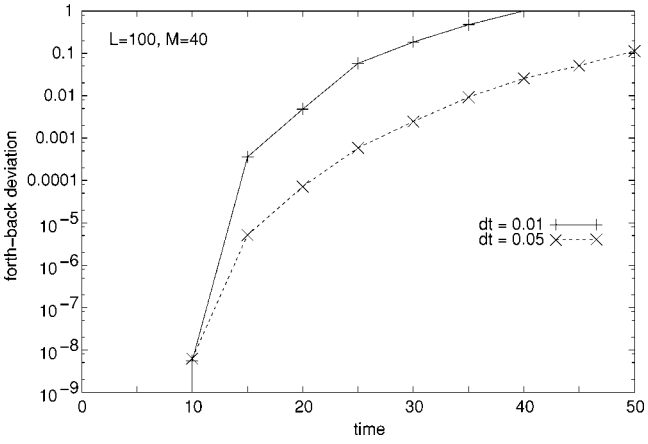

FIG. 7. The forth-back error $E_{\mathrm{FB}}(t)$ for $L=100$, $m=40$, $dt=0.01$, and $dt=0.05$ as a function of t.

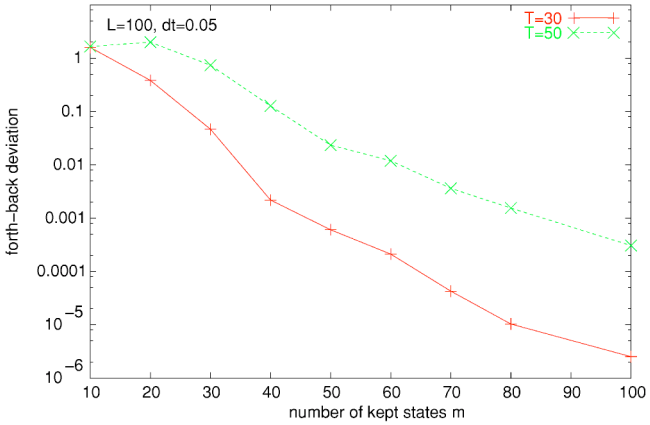

FIG. 8. The forth-back error $E_{\mathrm{FB}}(t)$ for $t=50$ and $t=30$ as a function of m. Here, $L=100$, $dt=0.05$.

might alternatively conceive that the well-defined runaway time t_R results from a sudden failure (of stochastic or of fundamental nature) of the truncation algorithm to capture one important basis state. It can be refuted on the basis of Fig. 5, Fig. 7, and Fig. 8: Such an error should manifest itself as a pronounced step in $E_{\mathrm{FB}}(t)$, depending on the time evolution having gone past t_R or not. Such a step is, however, not observed.

t_R might also be thought to reflect a fundamental DMRG limit, namely a growth of the entanglement within the time-evolved state which the limited number of DMRG states m is not able to capture adequately at $t>t_R$. This scenario can be excluded by observing the strong dependence of t_R on the number of time steps, which this scenario cannot explain. Indeed, a study of the entanglement entropy between the left and the right half of the chain

$$S_e(t) = \mathrm{Tr}\,\hat{\rho}\log_2\hat{\rho}, \tag{11}$$

$\hat{\rho}$ being the reduced density matrix of the left (or equivalently the right) half of the chain, confirms this view: As shown in Fig. 9, $S_e(t)$ is only mildly growing with time and

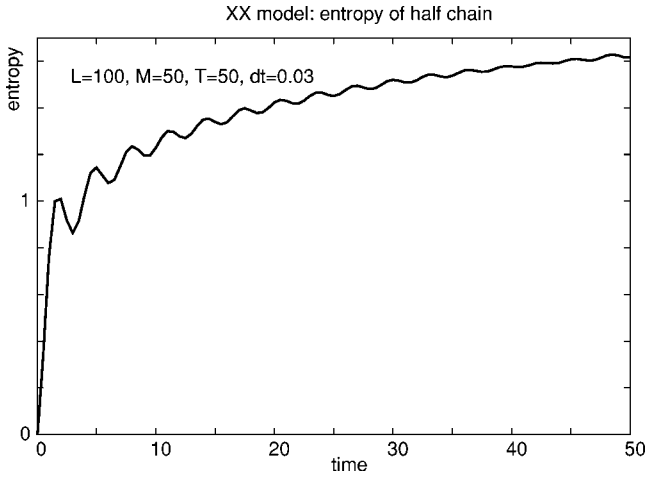

FIG. 9. Entanglement entropy S_e from Eq. (11) between the left and the right half of the chain as a function of time.

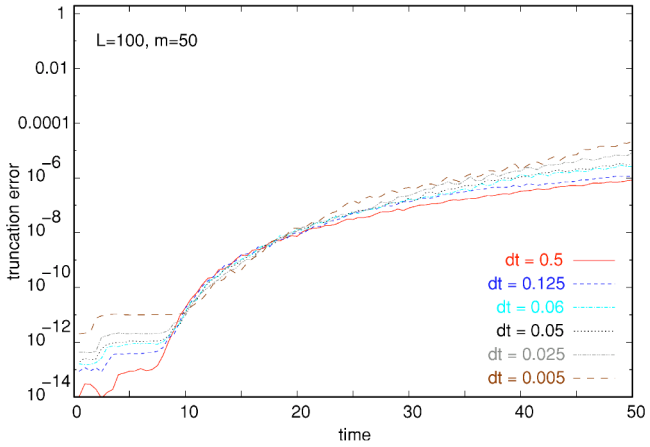

FIG. 10. The lost weight in the density matrix truncation, summed over time intervals $\Delta t=0.1$, is shown for the same parameters as in Fig. 3. A comparison with Fig. 3 reveals, however, that both values are not useful criteria for the DMRG truncation error and are in particular not suited to reveal the runaway time t_R.

is well below the maximum entanglement entropy $S_{\max}\sim\log_2 m$ that the DMRG can reproduce.

Therefore, we conclude that the error at short times is dominated by the Trotter error, which is independent of m and approximately growing linearly with time. At some runaway time, we observe a sharp crossover to a regime in which the m-dependent and almost exponentially growing truncation error is dominating. This crossover is sharp due to drastically different growth of the two types of errors. The runaway time thus indicates an imminent breakdown of the method and is a good, albeit very conservative, measure of available simulation times. We expect the above error analysis for the adaptive t-DMRG to be generic for other models. The truncation error will remain also in approaches that dispose of the Trotter error; maximally reachable simulation times should therefore be roughly the same or somewhat shorter if other approximations enhance the truncation error.

C. Optimal choice of DMRG parameters

How can the overall error—which we found to be a delicate balance between the Trotter and the accumulated truncation error—be minimized and the important runaway time be found in practice? From the above scenario, it should be expected that the truncated density matrix weight at each step does not behave differently before or after the runaway time and hence is no immediately useful indicator to identify the runaway time. This can in fact be seen from Fig. 10, where the truncated weight is shown for the same parameters as in Fig. 3. Also, it is not obvious to extract a precise relationship between the truncation errors at each DMRG truncation and the accumulated errors. Instead, a precise convergence analysis in m or dt seems to be more telling and easily feasible.

Of course, it is desirable to choose the number of kept states m as large as possible within the constraints regarding the available computer resources. This choice having been made, the runaway time t_R is determined for different Trotter

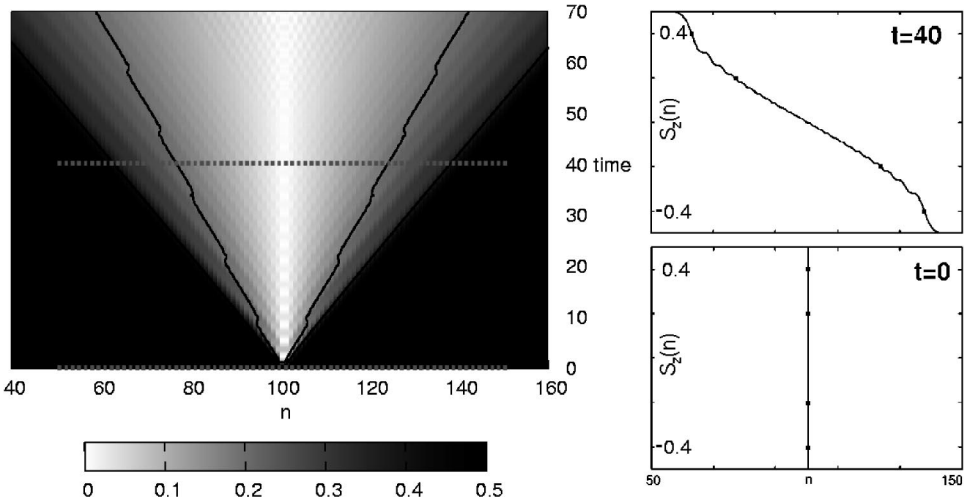

FIG. 11. Left: Time evolution of the absolute value of the local magnetization $|\langle S_n^z(t)\rangle|$ for the *XX* model as a density plot, where the local magnetization itself is exactly antisymmetric with regard to the chain center. The lines of constant magnetization $\langle S_n^z\rangle = \pm 0.2, \pm 0.4$ are shown as solid lines. As an illustration, local magnetizations $\langle S_n^z(t)\rangle$ for the time slices $t=0$ and $t=40$ are shown explicitly. A steplike substructure can be seen for $t=40$ in perfect quantitative agreement with the exact solution. Error bars are below visibility.

time steps *dt* by comparing different values of *m* as in Fig. 6. Only two slightly different values of *m* are sufficient for that purpose. Now the Trotter time step *dt* is chosen such that the desired time *t* is just below t_R. This way, the optimal balance between the Trotter error and the truncation error is found, which corresponds in the lower part of Fig. 4 to the minimum of err(*t*) on the border between regime A and B: The total error would increase at larger *dt* due to the Trotter error, and at smaller *dt* due to the truncation error.

Thus, it is a good practice to choose for small times rather small values of *dt* in order to minimize the Trotter error; for large times, it makes sense to choose a somewhat coarser time interval, in order to push the runaway time to as large values as possible.

In terms of numbers of time steps, we conclude from Fig. 3 that for the present model and our parameters ($L=100-200$), the adaptive time-dependent DMRG seems to be able to perform about 1000–5000 time steps reliably even for $m=50$, depending on the desired level of accuracy, corresponding to $O(100/J)$ in "real" time. We note that this is a very small value of *m* by DMRG standards, and that using an optimized code, one should be able to increase *m* by an order of magnitude, and hence access much longer times (by an order of magnitude).

V. LONG-TIME PROPERTIES OF THE TIME EVOLUTION

In [5,22], the time evolution of the initial state $|\mathrm{ini}\rangle$ on the *XX* chain at temperature $T=0$ was examined in the long-time limit using the exact solution. It was found that the magnetization $S_z(n,t)$ given in Eq. (4) can be described for long times in terms of a simple scaling function, $S_z(n,t)\approx\Phi[(n-n_c)/t]$, where n_c is the position of the chain center. The scaling function is the solution of the partial differential equation $\partial_t S_z+\partial_x j(S_z)=0$ with the magnetization current $j(S_z)=1/\pi\cos|\pi S_z|$ which has been shown to describe the macroscopic time evolution of the magnetization profile [5]. The characteristics, i.e., the lines of constant magnetization S_z, have a slope $v=\sin|\pi S_z|$.

The magnetization profile $\Phi[(n-n_c)/t]$ has a well-defined front at $(n-n_c)/t=\pm 1$, i.e., is moving outwards ballistically with velocity $v=1$. On top of this overall scaling form, an additional steplike substructure arises, which was analyzed in detail in [22]. It was found that while the step width broadens as $t^{1/3}$, the step height decreases as $t^{-1/3}$, such that the integrated transported magnetization within each step remains constant at 1. It was suggested that each of these steps corresponds to a localized flipped spin flowing outwards.

The *XX* model, however, has several very special properties: It corresponds to a free-fermion model and is therefore exactly solvable; it is critical; and its total current operator $J=\Sigma_n j_n$ commutes with the Hamiltonian, $[J,H]=0$. One may ask whether the above findings are due to any of the particularities of the *XX* model or more generic.

The adaptive t-DMRG allows us to study the long-time evolution of $|\mathrm{ini}\rangle$ in different coupling regimes of Eq. (1). We chose two extensions of the *XX* model, namely an S^zS^z interaction, and dimerization.

In Figs. 11 and 12, we visualize the time evolution of the local magnetization in density plots, with site index *n* on the *x* axis and time *t* on the *y* axis. Here, the absolute value of the magnetization is shown as a grayscale and in lines of constant magnetization at $|\langle S_z\rangle|=0.2$, 0.4. In Fig. 11, the relation between the density plots and the actual magnetization profile for the *XX* model is shown at two times, $t=0$ and $t=40$. The exact solution is perfectly reproduced, including the detailed substructure of the magnetization profile.

In Fig. 12, density plots for various values of J_z between 0 and 1.1 are shown. For small $J_z(J_z<1)$, we observe ballistic transport of the magnetization. This regime is characterized by a constant transport velocity of the magnetization, hence the lines of constant magnetization shown in Fig. 12 are approximately straight for $J_z<1$. The magnetization front propagation slows down as J_z increases, and almost comes to a halt when $J_z>1$. Although the sharpness of this crossover at $J_z=1$ is surprising, its general nature can be understood from the limits $J_z\to 0$ and $|J_z|\to\infty$: For small $J_z\to 0$, the S^xS^x and S^yS^y interactions dominate. Being spin-flip terms, they smear out the initially hard step profile in the *z* magnetization. For large J_z, on the other hand, the S^zS^z interaction dominates. This term does not delocalize the step profile, and in the limit $|J_z|\to\infty$, the initial state is even a stationary eigenstate of the Hamiltonian.

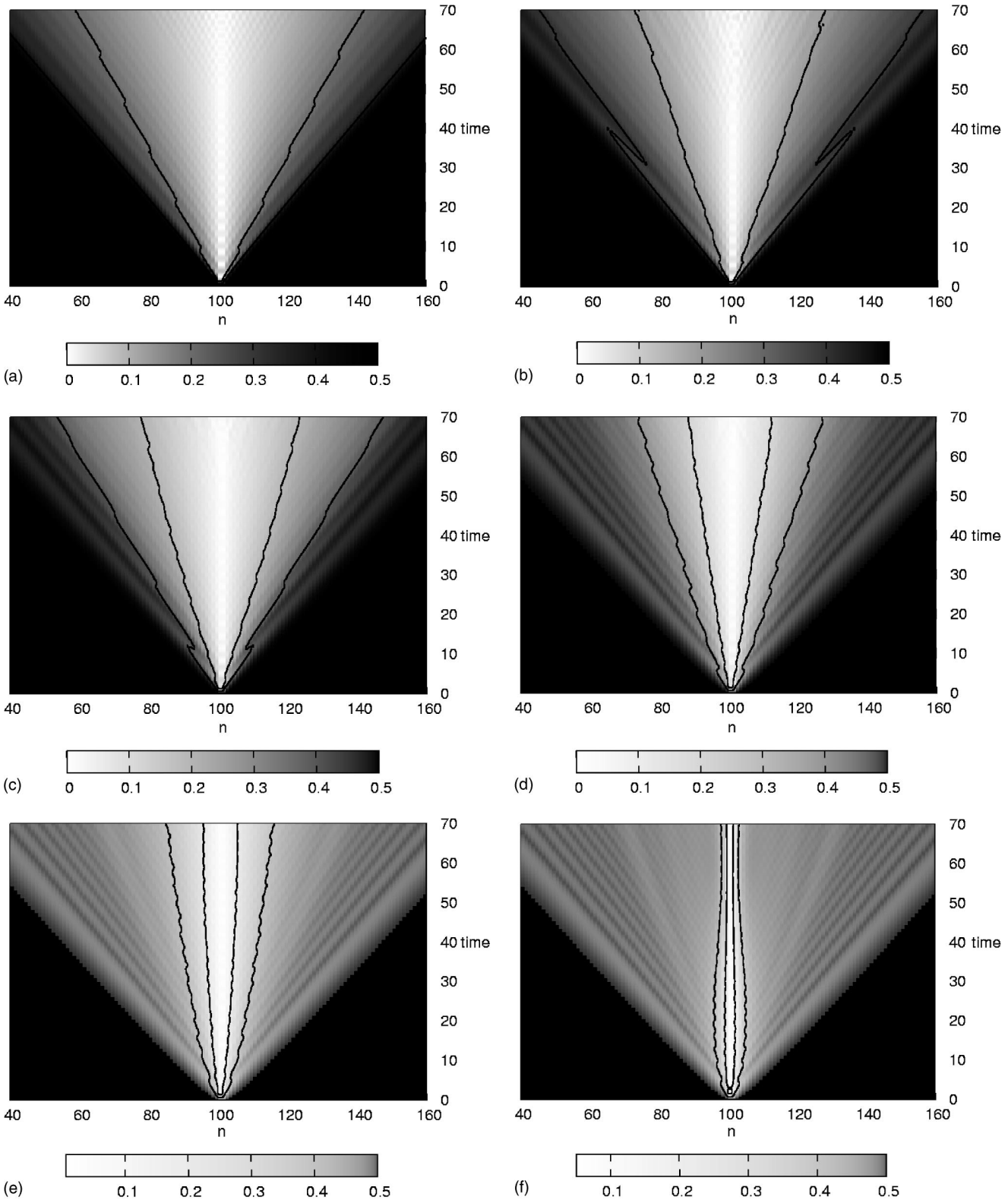

FIG. 12. Density plots of the magnetization $|\langle S_n^z(t)\rangle|$ as in Fig. 11, the values of J_z being (from left to right, top to bottom) 0, 0.3, 0.6, 0.9, 1.0, 1.1, and $\delta=0$. For better visibility of the profile, the grayscale mapping of $|\langle S_n^z(t)\rangle|$ was chosen differently in each plot as indicated by the legends. Solid lines: lines of constant magnetization $\langle S_n^z\rangle = \pm 0.2, \pm 0.4$; these allow for a direct comparison of the magnetization transport between different J_z. The raylike structure indicates the "carriers."

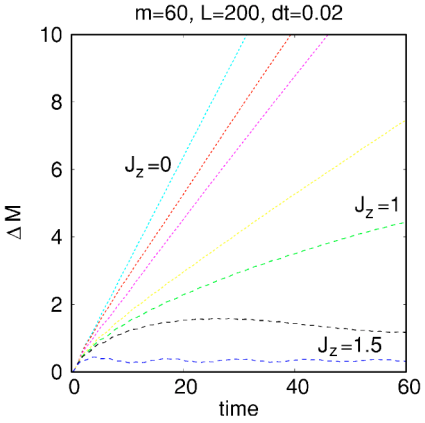

FIG. 13. The change in the magnetization $\Delta M(t)$ is shown. The curves are plotted in the order $J_z=0$, 0.3, 0.6, 0.9, 1.0, 1.1, and 1.5, where $J_z=0$ is the steepest. The curves $J_z=0$, 0.3, 0.6, and 0.9 show the same linear behavior for the observed times, i.e., up to $t=60$.

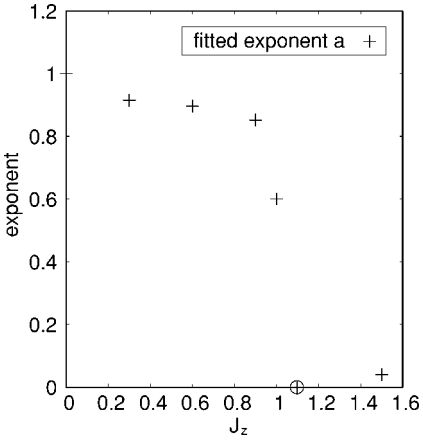

FIG. 14. Best fit for the exponent a in $\Delta M(t) \propto t^a$, for the data shown in Fig. 13 and for times between $t=20$ and $t=60$. We estimate the uncertainty in a to be of the order of 0.1 due to the limited time available (cf. Fig. 15). It was not possible to fit the slow oscillations for $J_z=1.1$. To the eye, however, the curve in Fig. 13 suggests slow oscillations around a constant value, hence we included in the data point $a=0$ for $J_z=1.1$ by hand (encircled).

Besides the structure of the overall front, we also observe for $J_z \neq 0$ remnants of the steplike substructure from the *XX* model, individual pockets of transported magnetization at velocity 1, which we call "carriers." As J_z is increased, these carriers keep the velocity $v \approx 1$, but are increasingly damped and thus less and less effective in transporting magnetization.

In order to put the above observations on a more quantitative footing, we plot in Fig. 13 the integrated flow of magnetization through the center,

$$\Delta M(t) = \int_0^t \langle j_{L/2}(t') \rangle dt' = \sum_{n>L/2}^{L} [\langle S_n^z(t) \rangle + 1/2]. \quad (12)$$

This quantity has the advantage that unlike the lines of constant magnetization in Figs. 11 and 12, it shows the overall spin transport without being too biased by single "carriers."

We observe in Fig. 13 roughly linear behavior of $\Delta M(t)$ for $|J_z|<1$, which suggests ballistic magnetization transport at least on the time scales accessible to us. As J_z increases, magnetization transport slows down until around $J_z=1$ the behavior changes drastically: For $J_z>1$, $\Delta M(t)$ seems to saturate at a finite value, around which it oscillates. On the time scales accessible to us, we thus find a sharp crossover at $J_z=1$ from ballistic transport to an almost constant magnetization.

This crossover is even more clearly visible in Fig. 14, where we plot the exponent a of the magnetization, $\Delta M(t) \propto t^a$, for values J_z between 0 and 1.5. Here, the exponent a is close to 1 for $J_z<1$, confirming the roughly linear transport, and quickly drops to zero in the regime of constant magnetization for $J_z>1$.

Figure 15 illustrates how the exponent a was obtained, for the special case $J_z=1$. Here the exponent $a=0.6\pm0.1$ indicates that the magnetization transport is clearly not ballistic anymore. In fact, we find from a scaling plot Fig. 16 that for long times the magnetization collapses best for a scaling function of the form $S_z(n,t) \sim \phi(n/t^{0.6})$ with an uncertainty in the exponent of approximately 0.1, indicating superdiffusive or diffusive transport in the time range under consideration.

The proposed crossover from ballistic to almost no transport is also visible in the expectation value of the current $j_n = J_n \mathrm{Im}(\langle S_n^+ S_{n+1}^- 0 \rangle)$. For $J_z=\delta=0$, it is known [5] that the current at the middle of the chain approaches a finite value as $t \to \infty$. This is only possible for ballistic transport. In the case of (sub/super)diffusive transport or constant/oscillatory magnetization, on the other hand, the central current must fall off to zero as the magnetization gradient flattens or must even become negative to allow for the oscillations.

This expected behavior is seen in Fig. 17, where we plot the current at the center of the chain as a function of time for various values of J_z between 0 and 1.1. We averaged the current over the five middle sites in order to filter out local current oscillations. We observe that for relatively long times, the current approaches a constant value for $|J_z|<1$, whereas the current falls off rapidly and then seems to exhibit damped oscillations around zero for $|J_z|>1$. This

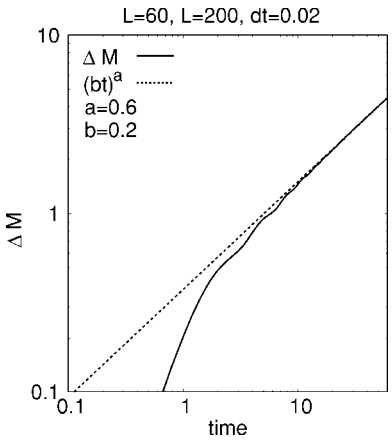

FIG. 15. $J_z=1$: The change of the magnetization in a double logarithmic plot with an algebraic fit.

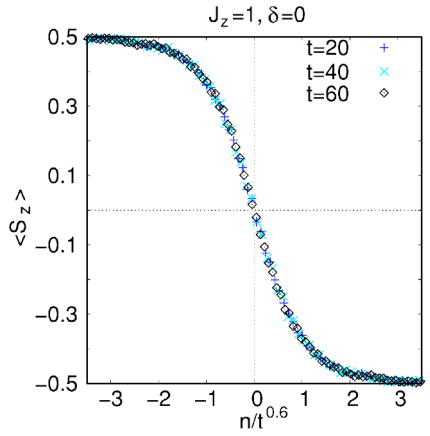

FIG. 16. $J_z=1$: Collapse of magnetization for a superdiffusive scaling form $(x/t^{0.6})$.

strengthens our previous conclusion of a crossover from ballistic transport to a more or less constant magnetization at $|J_z|=1$.

Remarkably, this crossover for the behavior of a high-energy quantum state $|\text{ini}\rangle$ is found at the location $J_z=1$ of the quantum phase transition from the critical phase to the Néel antiferromagnetic state (see Fig. 1), *a priori* a low-energy event. To understand the subtle connection between the time evolution of $|\text{ini}\rangle$ and the phase transition, we exploit that the time evolution does not depend on the sign of J_z, as discussed in Sec. II. Therefore, the time evolution of the high-energy state $|\text{ini}\rangle$ for $J_z>1$ is identical to that for $J_z'=-J_z<-1$, where $|\text{ini}\rangle$ is a low-energy state. At the quantum phase transition from the ferromagnetic state to the critical phase at $J_z'=-1$, the ground state, a kink state for $J_z'<-1$ (if we impose the boundary condition spin up on the left boundary and spin down on the right boundary) [14], changes drastically to a state with no kink and power-law correlations for $J_z'>-1$. Therefore, our initial state is very close to an eigenstate—the ground state—for $J_z'<-1$, but not for $J_z'>-1$. Thus, the harsh change in the time evolution of the high-energy state $|\text{ini}\rangle$ at $J_z=1$ can be explained by the severe change in the ground-state properties at $J_z'=-1$, and the crossover is linked to a quantum phase transition at a different location in the phase diagram.

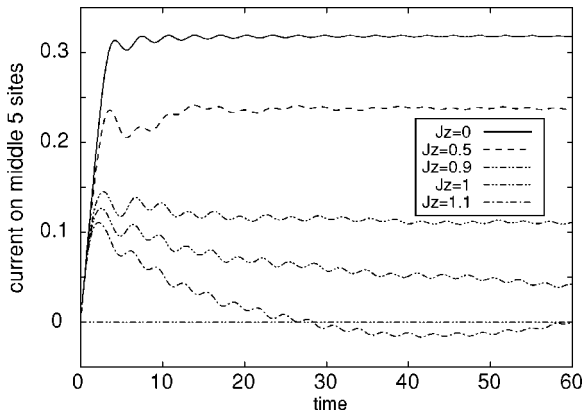

FIG. 17. Current, averaged over the five middle sites, for various values of J_z between 0 and 1.1.

We now study the influence of a nonzero dimerization δ in Eq. (1). We restrict our analysis to the case $J_z=0$. The dimerized models can still be described in terms of the free-fermion picture and are exactly solvable (for static properties, see [12]). The current, however, is not conserved for nonzero dimerization. This example will shed light on the question of whether the long-time limit depends on current conservation or on the free-fermion property, or on yet other special properties of the system. As the dimerized case is also exactly solvable, the results could have been obtained also analytically, for example by utilizing the results for the Fourier transformation of the magnetization $\langle S_z(q,t)\rangle$ of Ref. [6]. We expect two obvious effects of nonzero dimerization. First, the overall front velocity should slow down, because the magnetization now propagates faster on half of the links, but slower on the other half, the net effect being a reduction of the total velocity. Secondly, we expect oscillations with a period of two lattice sites. This is obvious in the limit $\delta\to 1$, where each strongly coupled pair of sites can be viewed as an almost isolated subsystem, in which the magnetization oscillates back and forth. We expect remnants of this behavior also at dimerizations $|\delta|<1$.

The data shown in Fig. 18 confirm this expectation qualitatively, but do not reveal any other qualitative change of the long-time limit for nonzero dimerization. For $\delta=1$, the system is trivially given by isolated pairs of neighboring sites, therefore the propagation velocity drops to zero.

Figures 19 and 20 reveal explicitly that no qualitative change occurs as the dimerization is switched on: the change in magnetization $\Delta M(t)$ still shows the linear behavior typical of ballistic transport. For increasing $\delta\to 1$, oscillations on top of this linear behavior arise. We find that switching on finite dimerization does not change the long-time behavior of the time evolution also for nonzero J_z (not shown). In particular, the time evolution here is drastically influenced by the transition at $J_z=1$, as in the case $\delta=0$ discussed above.

To summarize, we find the same long-time behavior of the initial state $|\uparrow\cdots\uparrow\downarrow\cdots\downarrow\rangle$ in the dimerized system—a system with a gapped excitation spectrum and which is exactly solvable—as in the system with small S^zS^z interaction, $|J_z|<1$—a system which is critical—whereas the behavior changes drastically for larger S^zS^z interaction, $|J_z|>1$. Hence we cannot attribute the ballistic transport of the magnetization to the specific properties of the XX model, neither to being exactly solvable, nor to the continuous spectrum, nor to the conserved current in the XX model. The drastic change at $|J_z|=1$ stems from the special property of the initial state to resemble the ground state in the ferromagnetic phase and the highest-energy state in the antiferromagnetic phase.

Finally, let us include a note on the errors in the present analysis. A convergence analysis in m as in Sec. IV shows that the errors and the runaway time are roughly the same as for the XX model. The plot in Fig. 12 goes up to time $t=95$, whereas the runaway time t_R is somewhat earlier, $t_R\approx 60-80$, depending on the precise value of J_z. Indeed, a convergence analysis in m reveals that the accuracy in the central region decreases for $t>t_R$. For dimerized models, the runaway time t_R is somewhat shorter (between $t_R=40$ and $t_R=80$ for $m=50$, depending on the dimerization). This fact reflects the reduced accuracy of the DMRG algorithm when

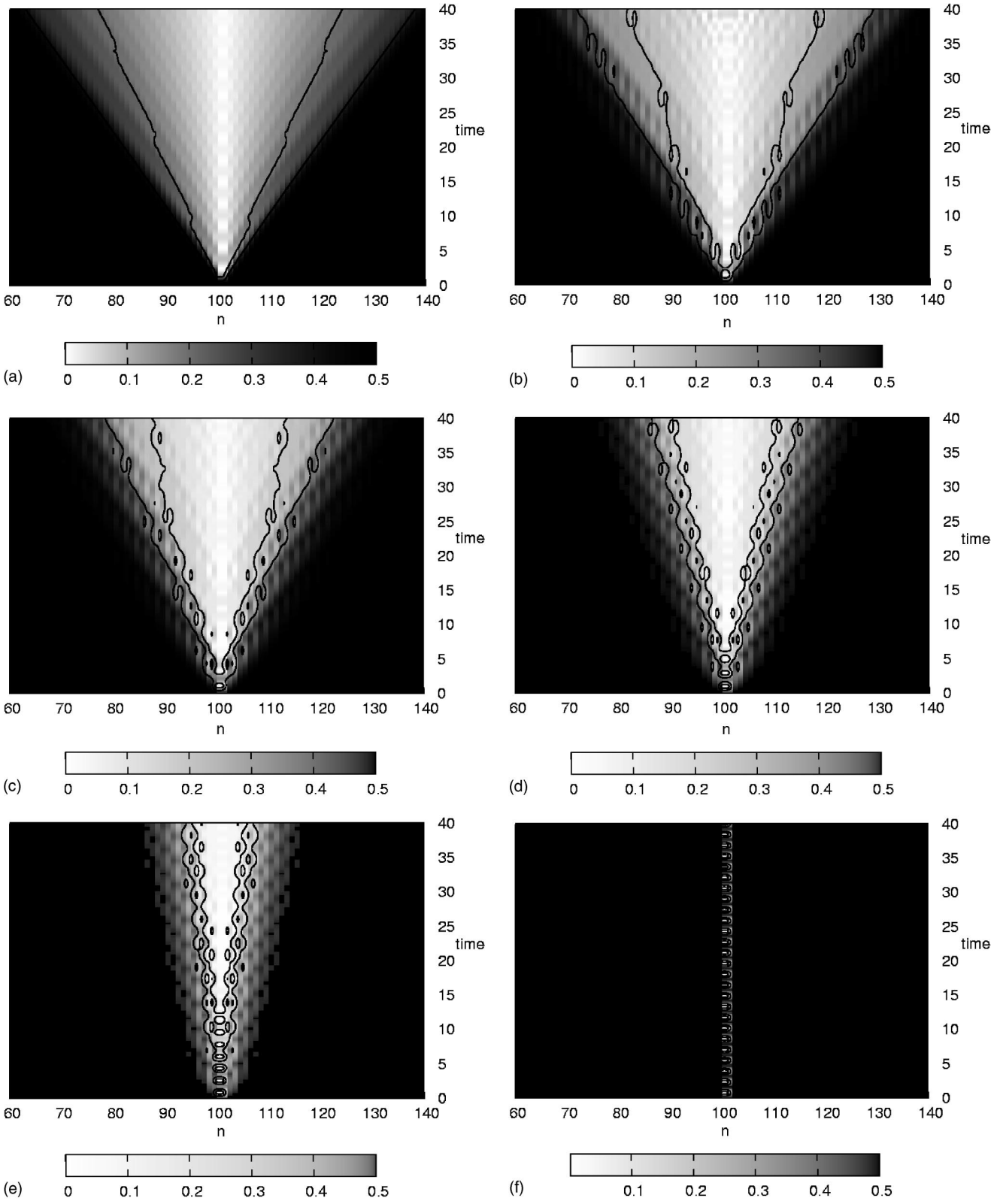

FIG. 18. Density plots of the magnetization $\langle S_n^z(t)\rangle$ as in Fig. 12, for dimerization (from left to right, top to bottom) $\delta=0$, 0.2, 0.4, 0.6, 0.8, 1.0, and $J_z=0$. The grayscale mapping is different in each plot as indicated by the legends. Solid lines: lines of constant magnetization $\langle S_n^z\rangle=\pm 0.2,\ \pm 0.4$.

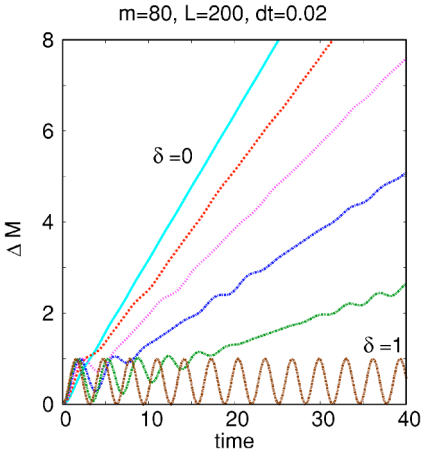

FIG. 19. Change in magnetization $\Delta M(t)$ for different dimerizations, from top to bottom: $\delta=0$, 0.2, 0.4, 0.6, 0.8, and 1.0.

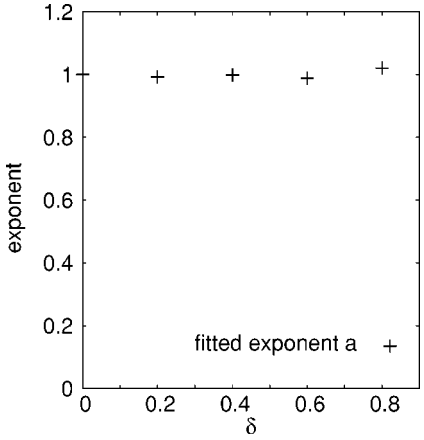

FIG. 20. Best fit for the exponent a in $\Delta M(t) \propto t^a$, for the data shown in Fig. 13 and for times between $t=20$ and $t=40$.

dealing with inhomogenous systems. As always, it is possible to increase t_R by increasing m.

VI. CONCLUSIONS

We have investigated the evolution of the initial state $|\uparrow \cdots \uparrow \downarrow \cdots \downarrow\rangle$ under the effect of nearest-neighbor interactions with the adaptive time-dependent DMRG.

For weak S^zS^z interaction, i.e., $|J_z|<1$ in Eq. (1), and arbitrary dimerization, $0 \leqslant \delta < 1$, we find that for long times the transport of the magnetization is ballistic as it was found for the XX model [5]. The magnetization profile shows the same scaling form for long times, i.e., $S^z(n,t)=\varphi[(n-n_c)/t]$, where n_c is the position of the chain center, but with different scaling functions φ. For stronger S^zS^z interaction, i.e., $|J_z|>1$, even in a homogeneous system, $\delta=0$, a drastic change in the long-time evolution is seen. The magnetization transport is no longer ballistic, but shows oscillatory behavior around a constant value. Hence our results suggest that the specific properties of the XX model are not responsible for ballistic transport at long times. The drastic change in the long-time behavior at the phase transition $J_z=1$ can be attributed to the close resemblance of the initial state to the ground state for $J_z<-1$.

Our error analysis for the adaptive time-dependent DMRG shows that for small times, the error is dominated by the Trotter error, whereas for long times, the truncation error becomes the most important. This finding should be general and hold for nonexactly solvable models as well, and should therefore allow us to control the accuracy of the results of adaptive time-dependent DMRG in general models. Overall, we find this method to be very precise at relatively long times.

ACKNOWLEDGMENTS

U.S. wishes to thank the Aspen Center for Physics, where parts of this work were completed, for its hospitality. The authors are grateful for discussions with Joel Lebowitz, Herbert Spohn, Hans-Jürgen Mikeska, Attila Rakos, Ian McCulloch, Zoltan Rácz, and Vladislav Popkov. C.K. and U.S. acknowledge support by the Studienstiftung des deutschen Volkes and the Young Academy, Berlin, respectively.

[1] A. Kuklov and B. Svistunov, Phys. Rev. Lett. **90**, 100401 (2003).
[2] L.-M. Duan, E. Demler, and M. Lukin, Phys. Rev. Lett. **91**, 090402 (2003).
[3] E. Altman, W. Hofstetter, E. Demler, and M. D. Lukin, New J. Phys. **5**, 113 (2003).
[4] O. Mandel, M. Greiner, A. Widera, T. Rom, T. W. Hänsch, and I. Bloch, Phys. Rev. Lett. **91**, 010407 (2003).
[5] T. Antal, Z. Racz, A. Rakos, and G. Schütz, Phys. Rev. E **59**, 4912 (1999).
[6] G. O. Berim, S. Berim, and G. G. Cabrera, Phys. Rev. B **66**, 094401 (2001).
[7] G. Vidal, Phys. Rev. Lett. **93**, 040502 (2004).
[8] A. Daley, C. Kollath, U. Schollwöck, and G. Vidal, J. Stat. Mech.: Theory Exp. P04005 (2004).
[9] S. White and A. Feiguin, Phys. Rev. Lett. **93**, 076401 (2004).
[10] S. White and A. Feiguin (unpublished).
[11] H.-J. Mikeska and A. Kolezhuk, in *Quantum Magnetism*, edited by U. Schollwöck, J. Richter, D. Farnell, and R. Bishop, Vol. 645 of Lecture Notes in Physics (Springer, Berlin, 2004), p. 1.
[12] G. Schütz, Phys. Rev. E **49**, 2461 (1994).
[13] E. Lieb, T. Schultz, and D. Mattis, Ann. Phys. (N.Y.) **16**, 407 (1961).
[14] H. Mikeska, S. Miyashita, and G. Ristow, J. Phys.: Condens. Matter **3**, 2985 (1991).
[15] S. White and R. Noack, in *Density Matrix Renormalization: A New Numerical Method in Physics*, edited by I. Peschel, X. Wang, M. Kaulke, and K. Hallberg (Springer, Berlin, 1999).

[16] U. Schollwöck, Rev. Mod. Phys. (to be published), e-print cond-mat/0409292.
[17] S. White, Phys. Rev. Lett. **77**, 3633 (1996).
[18] M. Suzuki, Prog. Theor. Phys. **56**, 1454 (1976).
[19] M. Cazalilla and J. Marston, Phys. Rev. Lett. **88**, 256403 (2002).
[20] F. Verstraete, J. Garcia-Ripoll, and J. Cirac, e-print cond-mat/0406426.
[21] F. Verstraete (private communication).
[22] V. Hunyadi, Z. Racz, and L. Sasvari, Phys. Rev. E **69**, 066103 (2004).